Instability of an idealized tidal mixing front: Symmetric instabilities and frictional effects

by K. H. Brink[1,2] and Deepak A. Cherian[1]

ABSTRACT

Finite amplitude instability of an idealized tidal mixing front is considered for cases where there is an active symmetric instability during the early stages of evolution. This can happen either when the initial front is sharp, or when a bottom stress leads to a well-mixed bottom boundary layer under the front. In either case, there is an initial phase, several days long, of slantwise convection, after which a much more energetic and spatially distributed baroclinic or barotropic instability dominates. The presence of an initial symmetrically unstable phase has no obvious effect on the subsequent eddy evolution. Bottom friction does lead to a slower growth rate for baroclinic instabilities, a lower eddy kinetic energy level, and (through stratified spindown) a tendency for flows to be more nearly surface intensified. The surface intensification means that the evolving eddy field cannot proceed toward a barotropic state, and so the horizontal eddy scale is also constrained. Thus, the finite-amplitude inverse cascade is strongly affected by the presence of a bottom stress. Scalings are derived for the frictionally corrected eddy kinetic energy and lateral mixing coefficient. The results, in terms of frictional effects on eddy structure and energy, appear to be valid beyond just the tidal mixing frontal problem.

1. Introduction

Tidal mixing fronts form at the boundary between stably stratified waters and regions where tidally generated turbulence mixes the water from surface to bottom. Thus, they are often found over continental shelves where tidal currents are particularly strong, such as in the Irish Sea or over Georges Bank (e.g., Simpson and Hunter, 1974; Loder *et al*., 1993). Idealized models suggest that these fronts can be baroclinically unstable (e.g., van Heijst, 1986; Thomas and Linden, 1996; James, 1989; Pasquet *et al*., 2012; and Brink, 2012). Both observations and more realistic numerical models also confirm that these fronts can be unstable around the British Isles (e.g., Simpson and James, 1986; Badin *et al*., 2009). The implications, especially in terms of enhanced lateral exchange, and parameter sensitivity of these instabilities are perhaps not so well understood. For this reason, a systematic study of this frontal instability was undertaken with the idea of ultimately assessing its biological

1. Department of Physical Oceanography, Mail Stop 21, Woods Hole Oceanographic Institution, Woods Hole, Massachusetts 02543, USA.
2. Corresponding author *e-mail: kbrink@whoi.edu*

impact. Brink (2012), on one extreme, treats the linear and nonlinear instability of an idealized initial front when there are no tides, bottom friction or symmetric instabilities. On the other hand, Brink (2013) treats more realistic cases that include tidal currents, bottom stresses, turbulent mixing and a simple biological model. Despite the differing assumptions in these studies, there are some broad points of agreement between these two approaches, such as the ubiquity of instability or the sensitivity to ambient stratification. This broad agreement suggests that realistic, lowest-order complications, such as an oscillating ambient current, do not fundamentally disrupt the instability process.

The present study aims to flesh out some of the issues at an intermediate level of complexity, leading to a better understanding of the more realistically complex frontal processes. First, the common thread in the new examples treated here is that they all undergo an initial phase of symmetric instability (e.g., Stone, 1966). These shear-driven instabilities occur when fQ becomes negative, where

$$Q = -\rho_z(v_x - u_y + f) + \rho_x v_z - \rho_y u_z \tag{1}$$

is the Ertel vorticity (ρ is density, f is the Coriolis parameter, u and v are horizontal velocity components in the x and y directions, and subscripts represent partial differentiation). These conditions can occur in zones of the tidal mixing front where horizontal density gradients are large, vertical shears are large, and/or stratification is weak. Similarly, within a bottom mixed layer below the front, similar conditions can also occur, especially in terms of weakened stratification. Second, the role of bottom friction is treated with an eye toward understanding how it affects stability and the longer-term evolution of the subsequent eddy field. In the more complex models of Brink (2013), bottom friction is present, but it is complicated by realistically oscillating "tidal" currents. Thus in the following, idealized numerical model experiments are used to treat, first, sharply defined fronts without bottom friction, and then cases that do include bottom friction. In both cases, the evolution of frontal instabilities is followed into the finite-amplitude range with attention to eddy kinetic energy levels and lateral mixing.

2. Approach

a. Model description and configuration

All model calculations are carried out using ROMS (Regional Ocean Modeling System) (e.g., Haidvogel *et al.*, 2000), a hydrostatic primitive equation numerical model that uses terrain-following coordinates. The equations of motion for the system are

$$u_t + uu_x + vu_y + wu_z - fv = -\rho_0^{-1}p_x + (Du_z)_z, \tag{2a}$$

$$v_t + uv_x + vv_y + wv_z - fu = -\rho_0^{-1}p_y + (Dv_z)_z, \tag{2b}$$

$$0 = -p_z - g\rho, \tag{2c}$$

$$u_x + v_y + w_z = 0, \tag{2d}$$

$$\rho_t + u\rho_x + v\rho_y + w\rho_z = (B\rho_z)_z, \tag{2e}$$

$$\rho = \rho_0[1 - \beta(T - T_0)]. \tag{2f}$$

In this system, u, v and w are the cross-channel, along-channel and vertical velocity components, and (x, y, z) are the corresponding coordinates. The pressure is p, T is temperature, ρ is density, t is time, f is the Coriolis parameter, ρ_0 is a constant reference density and g is the acceleration due to gravity. Subscripts with regard to independent variables represent partial differentiation. T_0 is a reference temperature (14°C), the thermal expansion coefficient for water is $\beta(1.7 \times 10^{-4}\,°\text{C}^{-1})$ and the vertical turbulent viscosity and mixing coefficients D and B, respectively, are found using the Mellor-Yamada level 2.5 turbulence closure scheme (e.g., Wijesekera *et al.*, 2003). There is no explicit lateral mixing or viscosity in any model run. The various symbols are defined in Table 1.

The model is configured as a cyclic (in y) channel bounded by solid walls at $x = 0$ and W. The depth h varies linearly across the channel:

$$h = H + \alpha(x - W/2), \tag{3}$$

where H is the mean depth and α is the bottom slope. As in Brink (2012), the model is initialized with a geostrophically balanced, idealized frontal structure that is meant to mimic the primary features of a tidal mixing front (Fig. 1):

$$\bar{\rho}(x, z) = \rho_0 \quad \text{for } x < W/2 - L, \tag{4a}$$

$$\bar{\rho}(x, z) = \rho_0 \left\{ 1 - \left[1 + \sin\left(\frac{\pi(x - W/2)}{2L}\right)\right] N_0^2 g^{-1}(z - z_0)/2 \right\}$$
$$\text{for } W/2 - L < x < W/2 + L, \tag{4b}$$

$$\bar{\rho}(x, z) = \rho_0 \left[1 - N_0^2 g^{-1}(z - z_0)\right] \quad \text{for } x > W/2 + L, \tag{4c}$$

so that

$$\bar{v}(x, z) = 0 \quad \text{for } |x - W/2| > L, \tag{5a}$$

and

$$\bar{v}(x, z) = \frac{\pi}{8fL} \cos\left[\frac{\pi(x - W/2)}{2L}\right] N_0^2(z + H)[(z - H) - 2z_0]$$
$$\text{for } |x - W/2| < L. \tag{5b}$$

In this notation, $\bar{\rho}$ is the initial density and $\bar{v}$ is the initial along-channel velocity. The initial constant buoyancy frequency on the stratified side of the front (larger x) is N_0. The frontal region is in the center of the channel (x between $W/2 - L$ and $W/2 + L$), and the water is vertically well mixed for $x < (W/2 - L)$. In addition, all runs are initialized with an additional small, random noise added to the surface elevation (typically of amplitude 10^{-4}

Table 1. Summary of symbols, with definitions and equation numbers.

| Variable	Meaning	Defining Equation Number
(u, v, w)	Velocity components	
(x, y, z)	Spatial coordinates	
ρ	Pressure	
t	Time	
f	Coriolis parameter	
Q	Ertel vorticity	(1)
N_0^2	Initial buoyancy frequency on the stratified side of the front	
W	Channel width	
L	Half width of the frontal region	
H	Mean water depth	
α	Bottom slope	
$-z_0$	Depth of maximum initial velocity	
β	Thermal expansion coefficient	
D	Vertical eddy viscosity	
B	Vertical eddy diffusivity	
r	Bottom resistance coefficient	
X	Representative cross-channel length scale	
Z	Vertical length scale	(17)
$eke(x, z, t)$	Local eddy kinetic energy per unit mass	(7a)
$MKE(t)$	Channel-averaged mean kinetic energy per unit mass	(7b)
$EKE(t)$	Channel-averaged eddy kinetic energy per unit mass	(7c)
EKE_M	Maximum (as a function of time) value of EKE	
$PE(t)$	Channel-averaged potential energy per unit mass	(7d)
APE	Channel-averaged available potential energy per unit mass	
$K(x, z, t)$	Horizontal eddy diffusivity, estimated from model outputs	(9)
$\Gamma(t)$	Baroclinicity diagnostic ($=0$ for barotropic flow)	(10)
λ	Along-channel wavelength of unstable disturbances	
$\bar{v}$	Initial along-channel velocity	(5a)
$\bar{\rho}$	Initial density	(4a)
$\overline{MKE}$	Channel-averaged initial kinetic energy per unit mass	
η	$(H + z_0) \, H^{-1}$	(12)
s	Slope Burger number: $\alpha N_0 f^{-1}$	(13)
S	Bulk Burger number: $N_0 H (fW)^{-1}$	(14)
d	Frictional parameter: $r(fH)^{-1}$	(15)
F	Rossby (Froude) number: $S\eta(WL)^{-1}/2$	(16)
Λ	Rossby radius length scale: $N_0 H f^{-1}$	
E_0	Scaling for EKE_M with no bottom friction: $APE(a + b|s|)^{-1}$	(20)
$S*$	$S(1 + \mu|s|\eta^{-2})$	(22b)
γ	Large-time frictional correction to E_0	(21b)
t_E	Time scale for eddy development: $2fL^2(\eta^2 N_0^2 H^2)^{-1}$	(24)
t_F	Time scale for eddy frictional decay: $fX(rN_0)^{-1}$	(23b)
q	Estimated ratio of eddy time scale to frictional time scale	(25)
σ	Total frictional correction factor for E_0	(26)
E_F	Scaling for frictionally adjusted EKE_M	(26)
K_H	Scaling for K: $E_F^{1/2}\Lambda\eta(1 + Cs^2)^{-1}$	(27)
a, b, c, C, G	Empirical constants	(20, 22a, 27)
μ, θ	Empirical constants	(22b, 25)
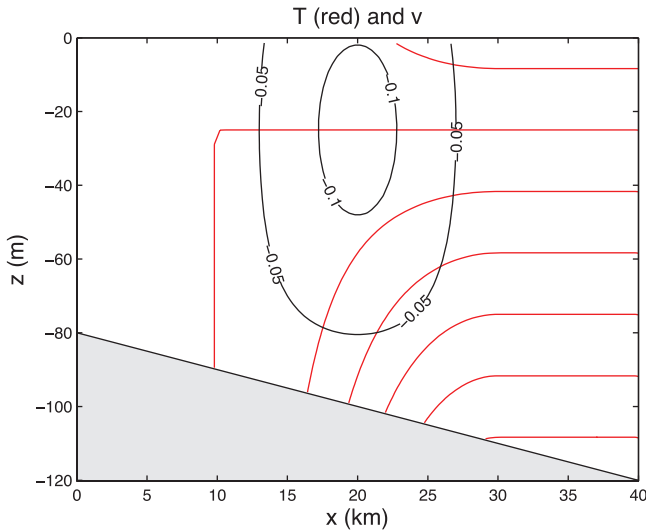
Figure 1. Initial along-channel velocity (black contours in m sec^{-1}) and temperature (red contour interval = 0.5°C) for model run 4. For this case, $H = 100$ m, $z_0 = -25$ m, $W = 40$ km and $L = 10$ km.

m) to help seed the instability. The depth of maximum along-isobath flow, $-z_0$, is varied, and the flow strengthens as the jet maximum approaches the surface. To aid in analyzing mixing, a passive tracer is also exploited. The tracer is initialized to be depth-uniform, and with the same smooth x dependence as density (4) at a depth $\neq -z_0$.

No stress is applied at the surface, and at the bottom, a linearized stress is allowed:

$$D(u_z, v_z) = r(u, v), \tag{6}$$

where r is a constant frictional coefficient. A free surface boundary condition is also applied. Side-wall boundary conditions are free-slip, and no heat flux is allowed through any of the boundaries.

The model is usually configured for a cyclic channel of length 100 km, and with cross-channel and along-channel grid resolutions of 0.4 and 0.25 km, respectively. The model is run with 30 levels in the vertical, stretched so as to concentrate points in the lower part of the bottom boundary layer. Local vertical resolution is thus typically coarser than 0.5 m and finer than 10 m.

A total of 36 new model runs are carried out (Tables 3 and 4), in addition to the 28 symmetrically stable, $r = 0$ runs in Brink (2012) (Table 2). Assessment of the impact of bottom friction is expedited by having 23 "twin" pairs that are identical except for whether $r = 0$ or not. In Tables 2 and 3, asterisks denote $r = 0$ runs that match one or more $r \neq 0$ runs.

Table 2. Summary of model runs with no bottom friction or symmetric instability. Asterisks denote runs that have one or more frictional twins (Table 4). Symbols are defined in Table 1.

Run	f $\sec^{-1}$ $\times 10^4$	H m	N_0^2 $\sec^{-2}$ $\times 10^4$	L km	W km	s	η	d	F	EKE_M $m^2 \sec^{-2}$ $\times 10^3$	K $m^{-2} \sec^{-1}$
1*	1.0	100	1.00	10.	40.	0	0.50	0	0.13	6.44	220
2*	1.0	100	0.50	10.	40.	0	0.75	0	0.20	5.46	545
3*	0.5	100	0.50	10.	40.	0	0.50	0	0.18	3.17	270
4	1.0	100	0.50	10.	40.	0.07	0.75	0	0.20	2.87	230
7*	1.0	100	0.50	10.	40.	0.07	1.00	0	0.35	8.32	420
9	1.0	100	0.50	10.	40.	0.04	0.75	0	0.20	3.79	525
12	1.0	100	0.50	10.	40.	0.11	0.75	0	0.20	2.09	130
13	1.0	100	1.00	10.	40.	0.15	0.75	0	0.28	4.23	430
15	1.0	100	0.50	10.	40.	−0.07	0.75	0	0.20	8.03	810
16	1.0	50	0.50	10.	40.	0	1.00	0	0.18	3.01	330
17	1.0	100	1.00	10.	40.	0.25	0.75	0	0.28	2.25	170
18	1.0	100	0.50	10.	40.	0.18	0.75	0	0.20	1.06	80
19*	1.0	100	1.00	10.	40.	0.25	0.50	0	0.13	1.74	150
20	1.0	100	0.50	10.	40.	0.18	1.00	0	0.35	3.40	280
21	1.0	100	0.50	10.	40.	−0.18	0.75	0	0.20	6.48	110
22*	1.0	100	0.50	20.	40.	0	0.50	0	0.04	2.22	190
23*	1.0	100	0.25	10.	40.	0	0.75	0	0.14	2.84	280
24	1.0	100	0.12	10.	40.	0	0.75	0	0.10	1.21	40
26*	1.0	100	0.50	10.	40.	−0.28	0.75	0	0.20	5.03	50
27	1.0	100	0.50	10.	40.	0.28	0.75	0	0.20	0.34	6
28	1.0	150	0.50	10.	40.	0.46	0.67	0	0.24	1.07	35
30	1.0	200	0.50	10.	40.	0.64	0.63	0	0.28	2.36	40
31	1.0	100	0.50	10.	40.	−0.13	0.75	0	0.20	6.12	190
32	1.0	100	0.25	10.	40.	−0.20	1.00	0	0.25	5.24	70
33*	1.0	100	0.50	10.	20.	0	0.75	0	0.20	3.71	125
34*	1.0	100	0.50	10.	40.	0.18	0.50	0	0.09	0.77	90
35*	1.0	100	1.00	10.	20.	0.15	0.50	0	0.13	2.73	180
36*	0.5	100	1.00	10.	20.	0.30	0.75	0	0.56	4.40	100

b. Diagnostics

In addition to the Ertel vorticity (1), the various energy pools and their transfers are used as diagnostics. Specifically, variables are averaged in the along-channel direction (denoted as $\{q\}$, where q is some quantity), and deviations from this mean are denoted as q'. The local eddy kinetic energy per unit mass is given as

$$eke(x, z) = \frac{1}{2} \left\{ u'^2 + v'^2 \right\}. \tag{7a}$$

Table 3. Summary of symmetrically unstable model runs with no bottom friction. Asterisks denote runs that have one or more frictional twins (Table 4). Symbols are defined in Table 1.

Run	f sec^{-1} $\times 10^4$	H m	N_0^2 sec^{-2} $\times 10^4$	L km	W km	s	η	d	F	EKE_M m^2 sec^{-2} $\times 10^3$	K m^{-2} sec^{-1}
40	1.0	100	1.00	10	40	0	0.75	0	0.28	11.99	770
41	1.0	100	1.00	10	40	0	1.00	0	0.50	28.59	1950
42*	1.0	100	0.50	10	40	0	1.00	0	0.35	12.62	510
43*	1.0	100	0.50	5	40	0	0.75	0	0.40	6.53	190
44	1.0	100	0.50	2	40	0	0.50	0	0.44	3.84	30
45	1.0	100	1.00	3	40	0	0.50	0	0.42	7.90	100
46	0.5	100	1.00	10	40	0	0.50	0	0.25	6.53	560
47	0.5	100	0.50	10	40	0	0.75	0	0.40	7.37	750
48	1.0	100	1.00	10	40	0.10	0.75	0	0.28	6.48	250
49	0.5	100	1.00	10	40	0.20	0.75	0	0.56	12.57	1050
50	0.5	100	1.00	10	40	0.50	0.75	0	0.56	4.81	480
51	0.5	100	1.00	10	40	0.50	0.50	0	0.25	2.75	220
52	1.0	100	0.50	10	40	−0.35	0.75	0	0.20	4.68	30

Averaged over the channel's cross-sectional area A, the mean kinetic energy, eddy kinetic energy and gravitational potential energy per unit mass are

$$MKE = \frac{1}{2A} \int_0^W \int_{-h}^0 [\{u\}^2 + \{v\}^2] dz dx, \tag{7b}$$

$$EKE = \frac{1}{2A} \int_0^W \int_{-h}^0 \{u'^2 + v'^2\} dz dx = \frac{1}{A} \int_0^W \int_{-h}^0 eke\, dz dx, \tag{7c}$$

$$PE = \frac{1}{\rho_0 A} \int_0^W \int_{-h}^0 \{g\rho z - g\rho_0 \xi_0\} dz dx. \tag{7d}$$

The constant reference level ξ_0 can be chosen arbitrarily. Note that this formulation does not lend itself to defining an eddy potential energy. The uncertainty of the *EKE* metric is estimated by executing repeated model runs with slightly different amounts of random initial noise. The peak (as a function of time) value of *EKE* (denoted by EKE_M) then varies over a range of about $\pm 20\%$ with these minor changes in initial conditions. We thus conclude that EKE_M is repeatable over about the same range.

The key energy conversions are those from potential to kinetic energy:

$$C_{PE \to KE} = -\frac{g}{\rho_0 A} \int_0^W \int_{-h}^0 \{w\rho\} dz dx, \tag{8a}$$

Table 4. Summary of model runs with nonzero bottom friction. Symbols are defined in Table 1.

Run	f sec^{-1} $\times 10^4$	H m	N_0^2 sec^{-2} $\times 10^4$	L km	W km	s	η	d	F	EKE_M m^2 sec^{-2} $\times 10^3$	K m^{-2} sec^{-1}
55	1.0	100	0.50	10	40	0	0.50	0.05	0.09	1.10	200
56	1.0	100	0.50	10	40	0	0.75	0.05	0.20	1.40	175
57	1.0	100	0.50	10	40	0	1.00	0.05	0.35	4.41	895
58	0.5	100	0.50	10	40	0	0.50	0.10	0.18	1.43	640
59	1.0	100	0.50	10	40	0	0.75	0.01	0.20	2.25	240
60	1.0	100	0.50	10	40	0	0.75	0.02	0.20	1.60	205
61	1.0	100	0.50	10	40	0	0.75	0.03	0.20	1.49	225
62	1.0	100	0.50	10	40	0	0.75	0.04	0.20	1.44	140
63	1.0	100	0.50	10	40	0.07	1.00	0.05	0.35	2.41	285
64	1.0	100	0.50	10	40	0.07	1.00	0.01	0.35	4.04	450
65	1.0	100	0.50	10	40	0	0.75	0.20	0.20	1.13	145
66	1.0	100	0.50	20	40	0	0.50	0.05	0.44	0.73	90
67	1.0	100	1.00	10	40	0	0.50	0.05	0.12	2.56	260
68	1.0	100	0.50	10	40	0	0.75	0.003	0.20	3.60	385
69	1.0	100	0.25	10	40	0	0.75	0.05	0.14	0.53	120
70	1.0	100	1.00	10	40	0.25	0.50	0.05	0.12	1.49	125
71	1.0	100	1.00	10	40	0.25	0.75	0.05	0.28	1.08	50
72	1.0	100	0.50	10	20	0	0.75	0.05	0.20	1.37	60
73	1.0	100	0.50	10	40	0.18	0.50	0.05	0.09	0.56	75
74	1.0	100	1.00	10	20	0.15	0.50	0.05	0.12	1.91	120
75	0.5	100	1.00	10	20	0.30	0.75	0.10	0.56	2.59	110
76	1.0	100	0.50	5	40	0	0.75	0.05	0.40	1.77	395
77	1.0	100	0.50	10	40	−0.28	0.75	0.05	0.20	1.85	110

and from mean to eddy kinetic energy:

$$C_{MKE \rightarrow EKE} = -\frac{1}{A} \int_0^W \int_{-h}^0 [\{v_x\}\{u'v'\} + \{v_z\}\{w'v'\} + \{u_x\}\{u'u'\} + \{u_z\}\{w'u'\}]dzdx.$$

(8b)

The first and third terms in (8b) are strongly associated with barotropic instability, whereas the second and fourth identify with shear (Kelvin-Helmholtz) instability. In general, the transfers associated with the mean cross-channel flow $\{u\}$ are found to be small.

As instabilities develop, there is an associated cross-channel eddy heat (or buoyancy) flux that varies with time in this initial value problem. We concentrate on fluxes at the moment of maximum cross-channel eddy heat flux, because this is a well-defined time indicative of baroclinic instability. Eddy fluxes of heat and a passive tracer at this moment are then used to estimate a lateral mixing coefficient K:

$$K = -\{u'T'\}\{T_x\}^{-1}.$$

(9)

Estimates at two depths (in the upper half of the water column) for the two variables are averaged to obtain a single estimate of K to characterize the strongest mixing phase of the instability. These estimates, reflecting a snapshot in time, are inherently noisy, and so a typical value is probably only reliable to within about $\pm 30\%$, on the basis of identical runs repeated with very small changes in initial conditions.

It is sometimes useful to characterize the degree of depth variation (baroclinicity) in the eddy horizontal currents. This is done following Brink (2012) using

$$\Gamma(t) = \frac{\left\{\sum_y \left[u'(W/2, y, 0, t) - u'(W/2, y, -h/2, t)\right]^2\right\}^{\frac{1}{2}}}{0.5 \left\{\sum_y \left[u'(W/2, y, 0, t) + u'(W/2, y, -h/2, t)\right]^2\right\}^{\frac{1}{2}}}, \tag{10}$$

where the sum is over all points along the length of the channel. For comparison, $\Gamma = 0$ for barotropic flow, and $\Gamma = 2$ for an $n = 1$ baroclinic mode with constant N^2. An along-channel wavelength λ is estimated using the cross-channel velocity component u in the upper half of the water column. Spatially lagged covariance functions for u are computed at a number of locations, and these are then averaged to obtain an energy-weighted spatial mean autocovariance function. The wavelength is taken to be four times the lag to the first zero crossing of this function, a choice consistent with the autocovariance function of a pure sinusoid. This is a natural scale definition, especially during the early phases of instability, when a single wavelength dominates.

c. Nondimensional parameters

It is straightforward to scale the system (2–5) to obtain useful nondimensional parameters (Brink, 2012). Depth is scaled by H, horizontal distances are scaled by an internal Rossby radius scale $\Lambda = N_0 H f^{-1}$, time by f^{-1}, velocity by V and density by $\rho_0 N_0 V g^{-1}$. (5b) shows that the velocity scale is then

$$V \approx \frac{(H + z_0)^2 N_0^2}{2 f L}. \tag{11}$$

The initial vertical structure is characterized by

$$\eta = (H + z_0) H^{-1}. \tag{12}$$

The effect of the bottom slope is characterized by the slope Burger number

$$s = \alpha N_0 f^{-1}, \tag{13}$$

and the water column effects of stratification by a bulk Burger number:
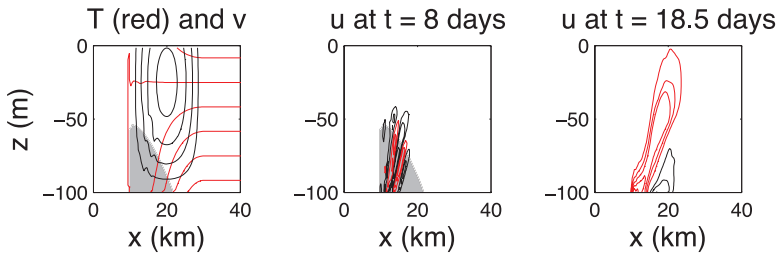
$$S = N_0 H (f W)^{-1}. \tag{14}$$

Figure 2. Results from model run 47 (symmetrically unstable, with no bottom stress) on day 8. Left panel: along-channel velocity (black contour interval $= 0.05$ m sec^{-1}; central contour $= 0.2$ m sec^{-1}) and temperature (red contour interval $= 0.5°$C). Center panel: cross-channel velocity (contour interval $= 0.005$ m sec^{-1}) with positive values in black and negative values in red. The area with negative initial Ertel vorticity (1) is shaded. Right panel: cross-channel velocity (contour interval $= 0.02$ m sec^{-1}) at day 18.5, when baroclinic instability dominates.

Finally, the gross effect of bottom stress is characterized by an Ekman-like number:

$$d = r(fH)^{-1}. \tag{15}$$

Thus, the Rossby (or Froude) number is

$$F = V(N_0 H)^{-1} = S\eta^2(W/2L), \tag{16}$$

where the second equality follows from (11) and (12). Thus, from the outset, spatial scales and kinetic energy levels are intimately related.

3. Results

a. Symmetric instability

i. No bottom stress. In the absence of bottom stress, the bottom boundary layer plays only the modest role of adjusting the bottom vertical temperature and velocity gradients to zero. Under these circumstances, the vorticity (1) is only modestly disturbed near the bottom. However, symmetric instabilities do occur when the interior horizontal velocity gradient becomes strong enough for Q to change sign somewhere. This typically happens on the less gravitationally stable side of the front, i.e., for $(W/2 - L < x < W/2)$, where ρ_z is small and v_z is substantial (see the shaded area in Fig. 2a,b). A total of 11 model runs were carried out in the category where Q changes sign and there is no bottom friction (Table 3).

Symmetric instabilities are typically detectable for several days before the more energetic baroclinic instabilities come into play. Slantwise convection is most apparent in the fields of cross-channel flow (Fig. 2), where there are tilted bands within and extending somewhat outside the region where $fQ < 0$. Typical horizontal velocities have a cross-channel wavelength of O (2–4 km) and are relatively weak: up to a few times 0.01 m sec^{-1}. Along-channel variations are negligible. Normally, the slantwise convection continues for O (5–10 days),

after which time the vorticity has adjusted to nearly neutral values, evidently by mixing with ambient waters having positive fQ. Next, baroclinic instability dominates, and the eddy field develops larger vertical and horizontal [O(10 km)] scales (e.g., Fig. 2c), velocity magnitudes of O(0.1 m sec^{-1}), and a tendency for the resulting eddies to be found all across the channel. Slantwise convection, although it temporarily dominates the cross-channel velocity, is thus not impressive energetically. Eddy kinetic energy, as defined by (7b), does not detect symmetric instabilities at all because its flow is uniform along-channel, but the u amplitude for slantwise convection (estimated using the cross-channel variance of $\{u\}$) is typically 1/10 or less of that for subsequent baroclinic instabilities. Further, the slantwise convection is spatially confined, and so its amplitude additionally pales in comparison to the widespread baroclinic eddies when averaged across the channel cross section. The symmetric instabilities are thus relatively weak and ephemeral and are rapidly replaced by far more energetic baroclinic or barotropic instabilities. In some cases, slantwise convection is clearly weakening before baroclinic instability reaches finite amplitude, but in other cases, baroclinic instabilities appear to overwhelm slantwise convection before the vorticity field has evolved to a neutral state.

The slantwise convection rolls often translate toward smaller x. For example, they move at about 0.6 km/day in run 41. This propagation occurs in the interior, with a flat bottom, and with no bottom stress, in contrast to the analogous propagating rolls of Allen and Newberger (1996, 1998) that occur in a bottom boundary layer over a sloping bottom. Recently, Pedlosky (2014) has shown that this roll translation can be explained by cross-channel variations in either the initial flow or the water depth.

Slantwise convection's ephemeral nature does not require that it have little impact. The small velocities, along with the short-length scales, still allow an eddy turnover time to be O(1 day), and the convection is clearly able to adjust the initial Q field toward a symmetrically stable state. However, integrated potential energy for run 47 (e.g.) over the symmetrically active time range of 3–12 days (Fig. 3) shows no noticeable change during the slantwise convection. Looking more closely at this run, mixing tied to symmetric instability raises the channel's center of gravity by 0.0005 m, or, equivalently, it changes the channel-averaged available potential energy (*APE*) by less than 0.4%. (Here, *APE* is estimated as the difference between *PE* at an early time and that at the moment of peak *EKE*.) This lack of impact was also found by Allen and Newberger (1998), who show that slantwise convection does not noticeably affect potential energy in their two-dimensional system. Thus, one might not expect symmetric instabilities to affect subsequent baroclinic instabilities. Indeed, analysis (see section 4.b) confirms that runs with and without an initial phase of slantwise convection obey the same scalings for the maximum eddy kinetic energy that results from purely baroclinic instability.

ii. With bottom stress. When the bottom stress is nonzero, the bottom boundary layer plays a good deal more active role. Finite bottom stresses lead to more active mixing beneath the frontal region, hence weaker vertical temperature gradients over the 2- to 25-m thickness
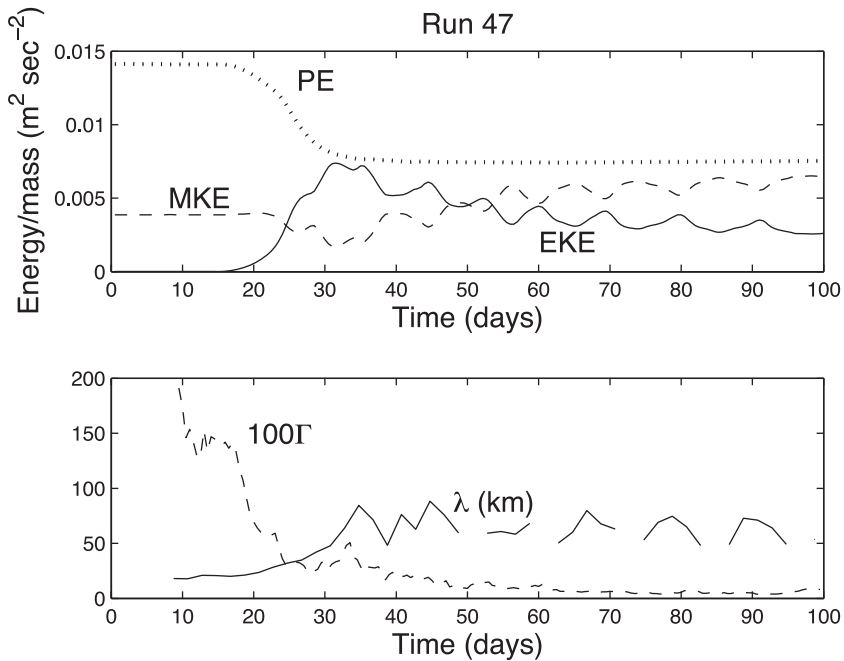
Figure 3. Results from model run 47. Upper panel: channel averages of potential energy (dotted line), mean kinetic energy (dashed line) and eddy kinetic energy (solid line). Lower panel: along-channel wavelength (in km; solid line) and the baroclinicity ratio Γ (10) multiplied by 100 for visibility.

of a bottom boundary layer. For the side of the jet with $x < W/2$, stratification is weaker than at larger x and a negative lateral shear v_x extends into the boundary layer, so that the term multiplied by ρ_z in (1) is relatively small. At the same time, the vertical gradient of along-isobath velocity v_z becomes more negative within the layer, while interacting with a largely undiminished positive horizontal density gradient ρ_x. The net effect is that, with nonzero friction, negative fQ rapidly develops within the bottom boundary layer so that runs with finite friction are invariably symmetrically unstable, at least within this confined thickness, prior to the onset of larger-scale instabilities in the overlying water column.

There are 19 model runs with $d \neq 0$ where the interior (above the bottom boundary layer) is in the symmetrically stable range (Table 4). Thus, the symmetric instabilities in these cases are entirely associated with bottom boundary layer processes. Of these runs, the cross-isobath wavelengths are typically in the range of 2–5 km, and the boundary layers are 2- to 25-m thick. The velocity amplitudes of the instabilities vary from run to run over the range of about 0.0001 m sec^{-1} to 0.02 m sec^{-1}. Whether the bottom slopes or not, the instability rolls translate toward smaller x, i.e., in the Allen and Newberger sense opposite to Ekman transport. Slantwise convection typically goes on for about 5–10 days, and it largely removes negative fQ, evidently through bottom dissipation. The evidence for
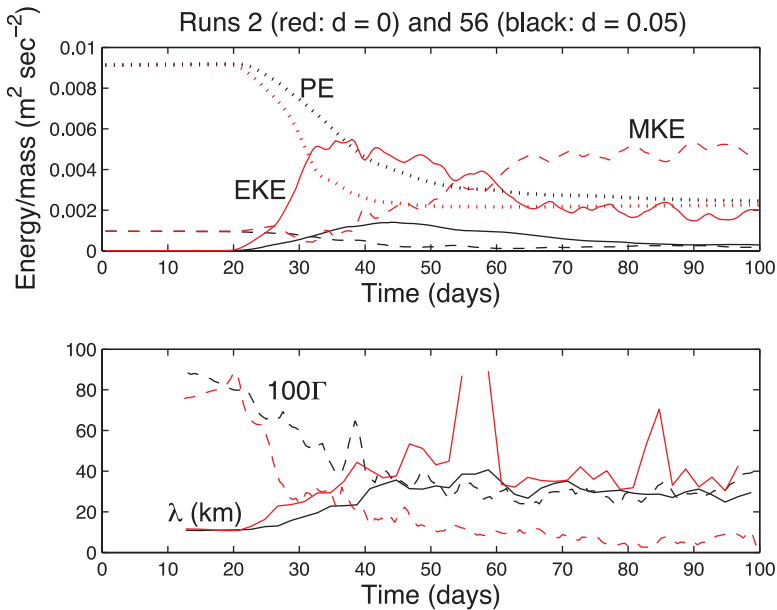
Figure 4. Results from model runs 2 ($d = 0$; red lines) and 56 ($d = 0.05$; black lines). These runs are identical except for the presence of bottom friction. Upper panel: channel averages of potential energy (dotted lines), mean kinetic energy (dashed lines) and eddy kinetic energy (solid lines). Lower panel: along-channel wavelength (in km; solid lines) and the baroclinicity ratio Γ (10) multiplied by 100 for visibility.

this conclusion is that the bottom boundary layer Q eventually becomes larger than that in ambient waters: an outcome inconsistent with mixing into the interior. More energetic interior baroclinic instabilities can sometimes grow rapidly enough to overwhelm slantwise convection before it has run to completion. As in the case with no bottom stress, the evolving slantwise convection makes no appreciable change in the system's potential energy. Finally, when interior (above the bottom boundary layer) conditions are symmetrically unstable as in run 57, the addition of bottom friction has little effect on the flow evolution.

b. Frictional effects on eddy evolution

The more important role of bottom friction in the instability process lies in its effect on the eddy field that results from baroclinic/barotropic instability. Friction is never found to prevent an actual instability, a result not inconsistent with the known tendency for bottom friction to enhance baroclinic instability at shorter wavelengths (e.g., Holopainen, 1961; Barth, 1989).

As an example, compare two runs (2 and 56) that are identical except that run 56 has a nonzero bottom stress, $d = 0.05$. The two cases start out with identical potential and mean kinetic energy (Fig. 4), and the instabilities reach finite amplitude at about the same time.
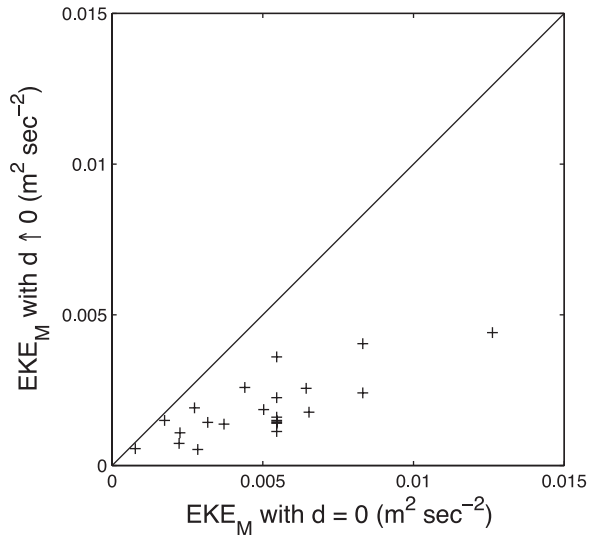
Figure 5. Maximum channel-averaged eddy kinetic energy per unit mass (EKE_M) for paired model runs that are identical except for the presence of a bottom stress.

However, the $d = 0$ run reaches a substantially higher peak eddy kinetic energy, and at an earlier time, than is the case in the more dissipative run. This decrease in EKE_M is, not surprisingly, a general result (Fig. 5). Similarly, initial growth rates (defined as the maximum rate from a moving 3-day exponential fit to the *EKE* time series) are generally greater by a factor of about 1–5 when $d = 0$. Rather strikingly, the subsequent inverse cascade leads to enhanced mean kinetic energy in the $d = 0$ cases, whereas when $d \neq 0$, mean kinetic energy decreases with time. The ultimate mean flow is typically sheared laterally but does not resolve into jets as found, for example, on a beta-plane by Vallis and Maltrud (1993). By the last 20 days of the run, however, EKE is nearly constant in both cases. Also, the total change in potential energy is nearly the same by the end of the run in the two cases despite the dramatic differences in total kinetic energy levels. All $d = 0$ runs nearly (there is dissipation within the basin interior) conserve total energy, but runs with bottom friction always lose substantial total energy through the decrease of mean and eddy kinetic energy. Finally, in this example, the most energetic wavelength tends to be somewhat greater when $d = 0$ than with bottom friction, although, in both cases, λ increases with time until about the time of maximum *EKE*. The baroclinicity ratio Γ, although it decreases with time in both cases (Fig. 4), shows clear differences, with the case with no bottom stress being more barotropic (smaller Γ) after the onset of finite-amplitude instability. With bottom friction, the late-term eddy field is relatively surface-intensified (larger Γ), reminiscent of the 1.5 layer results of Larichev and McWilliams (1991). The scale differences reflect distinctly different outcomes of the inverse cascade with and without bottom friction.
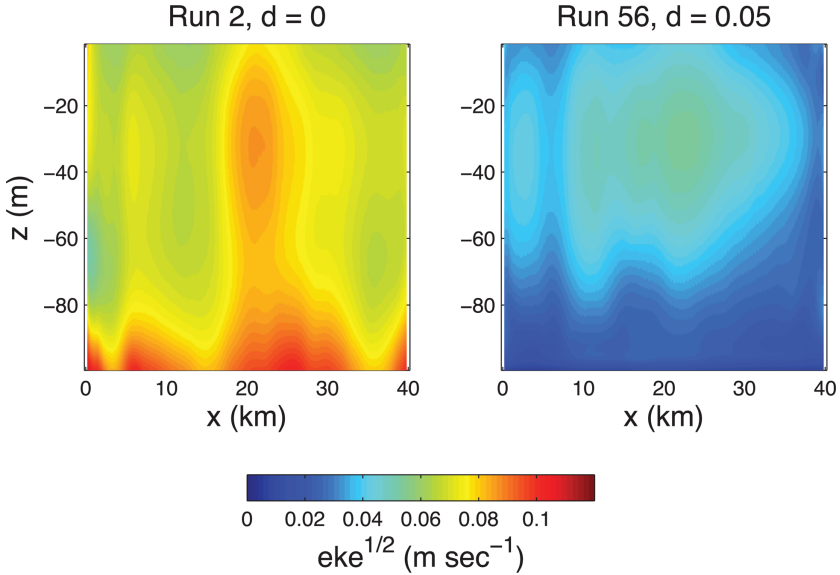
Run 2, d = 0   Run 56, d = 0.05

Figure 6. Eddy velocity magnitude (square root of local eddy kinetic energy: *eke*), averaged for the 3 days preceding maximum *EKE* for runs 2 and 56. The runs are identical except for the presence of a bottom stress.

Some further appreciation of the differences can be had from Figure 6, which shows a section of eddy kinetic energy *eke* computed for the 3 days preceding maximum *EKE* for runs 2 and 56. With no bottom friction (left panel), the maximum *eke* is at the bottom. For the run with friction, *eke* is everywhere smaller than in the $d = 0$ example. Further, with $d = 0.05$, the *eke* maximum is at about 30 m depth: 70 m above the bottom. Turbulent vertical stress gradient terms, however, are only appreciable within 10 m of the bottom, so the velocity (both mean and eddy) adjustments over the depth range 30–90 m are associated with thermal wind shear. With time, the $d = 0$ case evolves toward an increasingly barotropic state (consistent with a classic inverse cascade: $\Gamma = 0.07$), whereas with bottom stress, both mean and eddy currents remain clearly depth-dependent ($\Gamma = 0.31$).

This depth-dependent eddy field with $d \neq 0$ is, of course, to be expected from a stratified spin-down problem (Holton, 1965a, b; St. Maurice and Veronis, 1975) where only the lower part of the interior water column (i.e., immediately above the bottom boundary layer) is affected by the secondary circulation driven by the bottom stress. The thickness Z of the affected region is expected to scale as

$$Z = O(fXN_0^{-1}), \tag{17}$$

where X is a horizontal eddy length scale, which is left unspecified for the time being. This scaling is a straightforward consequence of interior vorticity conservation and thermal wind
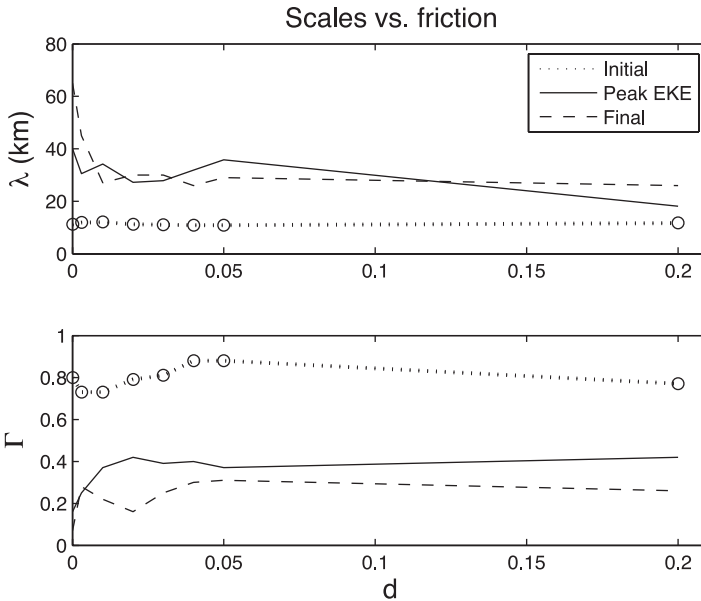
Figure 7. Dependence of eddy scales on the strength of bottom friction. All model runs are identical
  except for the magnitude of the bottom frictional parameter r. Shown are results from model runs
  2, 68, 59, 60, 61, 62, 63, 56 and 65. Upper panel: along-channel wavelength as a function of d at
  the outset of instability (dotted line and circles), at the time of peak instability (solid line) and for
  the last 10 days of the model run (dashed line). Lower panel: the baroclinicity ratio Γ as a function
  of d for the same three times.

balance. At distances greater than Z above the bottom, the flow evolves independently of
any direct effect of the bottom stress. This adjustment of the interior (above the bottom
boundary layer) flow structure to minimize the bottom stress occurs in several types of
linear wave problems (e.g., Allen, 1984; Power *et al.*, 1989; Brink, 2006). Further, Arbic
and Flierl (2004) demonstrate that a similar sort of adjustment occurs for nonlinear two-layer
quasigeostrophic eddy evolution.

LaCasce and Brink (2000) and Arbic and Flierl (2004) find that, for weak friction, the
equilibrated horizontal eddy length scale increases as friction decreases. This result is tested
here with a sequence of model runs that are all identical to run 2, but with varying bottom
frictional coefficient, r. The result for these runs (Fig. 7) is consistent with Arbic and Flierl
in that for the bottom friction parameter $d < 0.02$, the final length scale decreases as d
increases; for larger d, the scales do not decrease further. This dependence of length scale on
friction is intuitive in the sense that the flow cannot become barotropic if there is stratification
and bottom friction. Rather, surface intensification means that there are variations in z, so
that Z always remains finite. Equation (17), in turn, requires that the horizontal scale X
cannot grow indefinitely. Thus, vorticity conservation in the presence of a bottom stress
halts the inverse cascade and results in a shorter horizontal length scale than in the $d = 0$
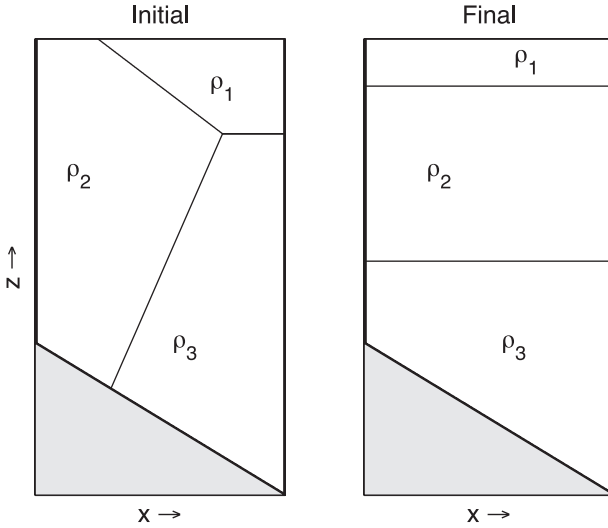
Initial   Final

Figure 8. Layered geometry for the estimation of initial (left) and final (right) potential energy. The estimated available potential energy, $< APE >$, is then the difference of these two potential energies (angled brackets represent an estimate based on this layered idealization).

case. Indeed, by the end of the model runs, the cases with friction are generally (all but one case) more baroclinic (for $d \neq 0$, Γ is always > 0.16, and usually in the range of 0.3–0.8) than the equivalent runs with no bottom stress (where the final Γ is often less than 0.1).

4. Scalings

a. Eddy kinetic energy with no bottom friction

Brink (2012) scales peak eddy kinetic energy with a crude estimate, based on a layered model, of available potential energy per unit mass (*APE*). His *APE* estimate encompasses only the frontal zone and ignores the bottom slope, but it has a conveniently analytical form:

$$< APE >= \frac{N_0^2 H^2}{48} \left[\eta^3 + (1 - \eta)^3 \right], \tag{18}$$

where the angle brackets ($< q >$) denote a quantity estimated using the layered approximation. A better approximation to the *APE* can be obtained using a somewhat refined version of the layer geometry that accounts for the bottom slope and the entire channel width (Fig. 8). Alternatively, the APE can be calculated exactly using (7d) by comparing the initial *PE* to that of a "resorted" density field that has flat isopycnals. Comparison of 41 independent examples shows that the two estimates agree well: a correlation of 0.96, with the layered model overestimating *APE* by about 30%. Initial kinetic energy $\overline{MKE}$ computed from the layered model also agrees comparably well with the exact result. Either
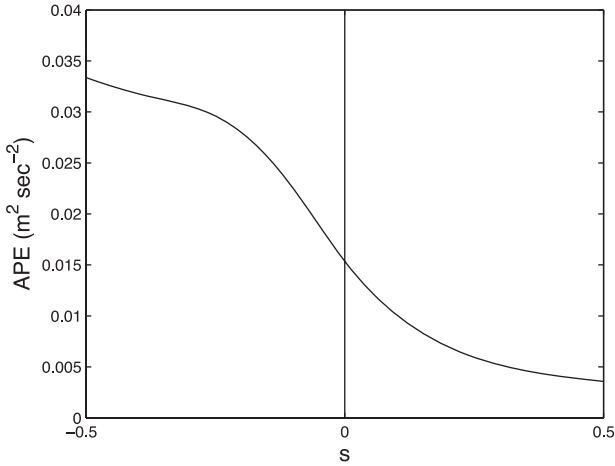
Figure 9. Initial available potential energy *APE* as a function of bottom slope, expressed as *s*. The calculation was carried out using parameters representative of run 40 but varying the bottom slope α. Positive s corresponds to an arrangement where stratified conditions occur in deeper water.

way, the estimate is made numerically, so the exact *APE* calculation is used throughout the following.

APE has a substantial dependence on the bottom slope (Fig. 9: presented as a function of the scaled slope, *s*). Brink's (2012) estimate would be roughly equivalent to using only the $s = 0$ value. As compared with the positive slope case, the case with negative bottom slope (deeper water on the homogeneous side of the front, which is decidedly aphysical in light of tidal amplitudes and mixing usually weakening in deeper water) has more *APE* and thus leads to a more energetic eddy field (compare run 4 with 15 or run 18 with 21 in Table 2, for example). Thus, accounting for the sloping bottom in computing *APE* can allow a more successful estimate of EKE_M.

Basing a scaling on *APE*, however, assumes that all of the *EKE* stems from a purely baroclinic instability, i.e., that $C_{PE \to KE}$ dominates the energy conversions. Diagnosis of energy evolution using (8) shows that, for a few runs (such as runs 49 or 50), barotropic instability ($C_{MKE \to EKE}$) dominates the energy exchanges after an initial period of symmetric instability. The runs with a substantial barotropic instability energy conversion are found to be those where $APE < 1.3 \, \overline{MKE}$. Of the remaining runs (with larger *APE*), the initial *APE* estimate is typically at least a factor of 5 larger than $\overline{MKE}$. It is straightforward, with a flat bottom, to use the velocity scale (11) along with the analytical Brink (2012) scale for *APE* (18) to estimate roughly the relative magnitudes of the energy pools for the tidal mixing front configuration:

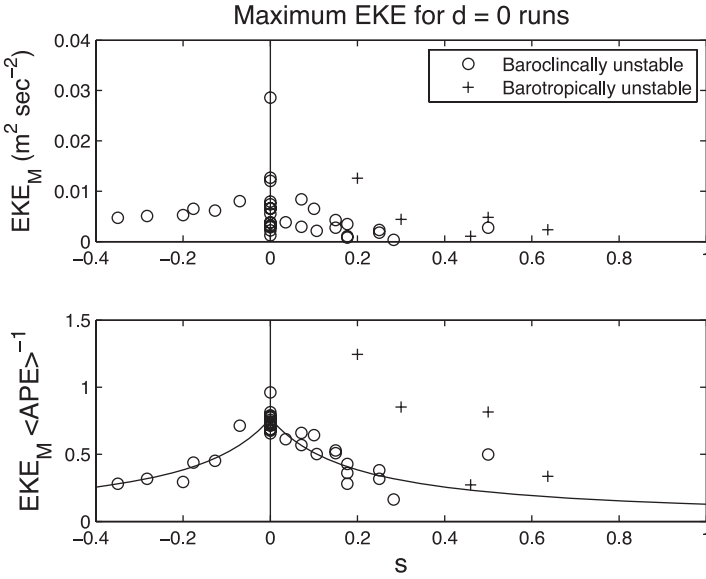$$\frac{\overline{MKE}}{APE} = O\left[S^2\eta^2\left(LW^{-1}\right)\right] \tag{19}$$

Figure 10. Maximum spatially averaged eddy kinetic energy per unit mass (EKE_M) as a function of s for runs with no bottom stress ($d = 0$). The circles are runs that are baroclinically unstable, whereas the + signs are runs where the instability is more nearly barotropic. Lower panel: EKE_M normalized by initial available potential energy APE. The solid line is $a(1+b|s|)^{-1}$, where $a = 0.57$ and $b = 6$, a line meant to fit the circles only.

Removing the 5 $d = 0$ runs with a substantial barotropic energy allows a relatively cleaner collapse of the model results (Fig. 10). An attempt to account for the barotropic instability, by scaling EKE_M by the sum of $\overline{MKE}$ and APE, does not improve matters any, perhaps because MKE by itself is not likely to provide much information about the fraction of MKE that is available for conversion to EKE. Once the APE scaling is applied for the baroclinically unstable cases, there remains a clear, slightly asymmetric, tendency for EKE_M to decrease with increasing $|s|$ (Fig. 10, lower panel). This tendency for the bottom slope to limit the peak eddy kinetic energy is accounted for empirically, so that the scaling for EKE_M is

$$E_0 = aAPE(1 + b|s|)^{-1}. \tag{20}$$

The physical meaning of the slope correction in (20) is clear in light of the Charney-Stern-Pedlosky criterion (Charney and Stern, 1962; Pedlosky 1964a,b), which states that quasigeostrophic baroclinic stability requires the isopycnals near a boundary to be parallel to that surface. The expected mean end state of eddy evolution with a flat bottom would be a stable configuration where all of the isopycnals are flat and the available potential energy is completely depleted. However, with a sloping bottom, the stable mean state might have

flat isopycnals in the interior, but stability requires that the deepest isopycnals slant to be parallel to the bottom. The tendency toward these end states is illustrated in Figure 10 of Brink (2012). Thus, with sloping boundaries, some available potential energy remains, and one can no longer equate initial available potential energy with the peak eddy kinetic energy. Rather, EKE_M ought to be less than APE when there is a sloping bottom.

The coefficients in (20) are found by least squares fitting on all 36 baroclinically unstable runs (i.e., with $APE > 1.3 \overline{MKE}$, corresponding to the circle symbols in Fig. 10) with $d = 0$. The resulting values of $a = 0.79$ and $b = 5$ give a correlation between E_0 and EKE_M of 0.99 and an rms error of 0.69×10^{-3} m^2 sec^{-2}. A somewhat better fit could be had by allowing a different b for positive and negative s.

Up to this point, no distinction in the EKE_M scaling has been made between cases that are initially symmetrically unstable or not. To check on this point, the scaling (20) is evaluated with $a = 0.79$ and $b = 5$ separately for the 25 $d = 0$ cases that are symmetrically stable and baroclinically unstable as compared with the 11 $d = 0$ cases that are symmetrically unstable and baroclinically unstable. The symmetrically stable runs obey (20) with a correlation of 0.96, and rms error of 0.59×10^{-3} m^2 sec^{-2}, whereas the symmetrically unstable runs yield a correlation of 0.99, and an error of 0.84×10^{-3} m^2 sec^{-2}. Taking a somewhat different approach, a is estimated separately using the two groups of runs: for the symmetrically stable runs, $a = 0.77 \pm 0.04$ (at 95% confidence) and for the symmetrically unstable runs, $a = 0.80 \pm 0.08$. By either test, the two groupings obey, with a high degree of confidence, the same scaling. The visual agreement (Fig. 11) is excellent as well. The finding that symmetric instability does not affect the EKE_M scaling strongly supports the conclusion that an initial symmetrically unstable phase does not affect the subsequent baroclinic instability and eddy evolution.

b. Accounting for bottom friction

For each of the 23 model runs with $d \neq 0$ (Table 4), there is a run that is identical except that $d = 0$ (Tables 2 and 3). This gives a basis for evaluating an EKE_M scaling that accounts for bottom friction by means of a few plausible conjectures.

As mentioned in the previous section, once the stratified spindown process has gone to completion, the vertical scale of the interior, spun-down region above the bottom boundary layer ought to be about $Z = fXN^{-1}$ (e.g., St. Maurice and Veronis, 1975), where X is an appropriate horizontal scale. This lateral scale is taken to be the channel width W, in the understanding that eddies tend to expand with time. The resulting vertical scale is naturally compared with the mean water depth in the channel, H. Thus, the bulk Burger number S representative of the entire channel (14) can be thought of as the ratio H/Z. As S approaches zero ("weak stratification"), the flow is expected to be relatively barotropic (large vertical scale compared with H), and so bottom friction should affect the entire water column. Thus, in this limit, one might expect that all motions are damped out and that $EKE \to 0$. On the other hand, as S becomes large, the portion of the water column affected
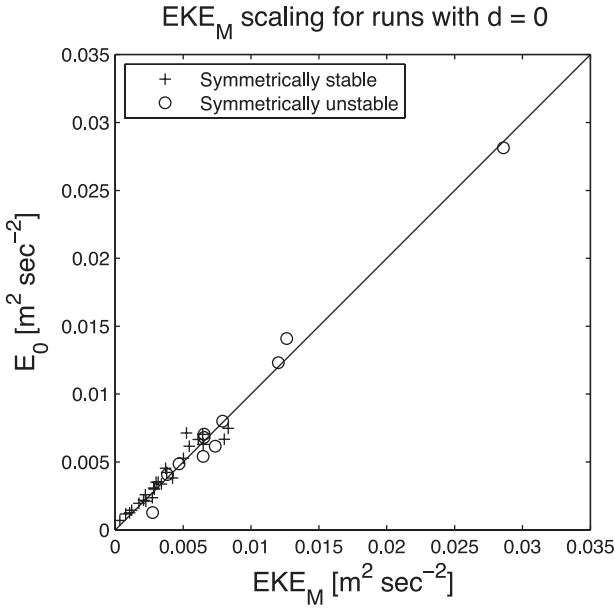
Figure 11. Comparison of computed maximum channel-averaged eddy kinetic energy per unit mass EKE_M with a scaling E_0 (20) for eddy kinetic energy. Only model runs that do not include bottom friction are used. Pluses are runs that do not have an initial phase of symmetric instability (i.e., the initial $fQ > 0$ everywhere), and circles represent runs that do have an initial phase of symmetric instability ($fQ < 0$ over some part of the initial domain).

by bottom friction becomes more and more confined near the bottom. Thus, for larger S, EKE_M might be expected to approach the $d = 0$ limit. After allowing for a long time for frictional adjustment, a scaling for EKE_M in the presence of bottom friction, E_F, might be proportional to the $d = 0$ estimate, so that

$$E_F = \gamma E_0. \tag{21a}$$

The frictional correction factor γ must have a functional form that obeys the expected behaviors for large and small stratification, such as

$$\gamma = cS(1 + cS)^{-1} \tag{21b}$$

(where c is an unknown constant), which is found to be an adequate formulation. Experimentation shows that better results are found if the bottom slope is accounted for by using the empirically determined form

$$\gamma = cS^*(1 + cS^*)^{-1}, \tag{22a}$$

where

$$S^* = S(1 + \mu|s|\eta^{-2}), \tag{22b}$$

μ being an empirical constant. The modification (22b) emphasizes that both the bulk strati-fication and the bottom slope affect the vertical scale over which stratified spindown occurs.

The argument leading to (21–22), however, assumes that frictional adjustment has run to completion by the time EKE_M is reached. In reality, near-bottom spindown takes a finite time

$$t_F = O(Zr^{-1}), \tag{23a}$$

or, using (17),

$$t_F = O\left[fX(rN_0)^{-1}\right], \tag{23b}$$

where X is a horizontal length scale and Z is the thickness of the layer being influenced by friction through secondary circulations. It then seems reasonable to expect that EKE is diminished as $exp(-2t/t_F)$ by frictional decay. Thus, at times short compared to t_F, the EKE ought to be largely unaffected by bottom friction. Only if EKE_M is reached after a time large compared to t_F will the limit (22) apply. One might expect that the time to reach EKE_M would scale like an eddy turnaround time, i.e., an eddy horizontal scale divided by an eddy speed: $t_E = O(X/V)$. For this purpose, the initial frontal half-width L is found to be a good choice for the eddy scale X. Thus

$$t_E = 2fL^2(\eta^2 N_0^2 H^2)^{-1} \tag{24}$$

from (11) and (12). Given these eddy and frictional time scales, dissipation can be accounted for through a factor of e^{-q}, where

$$q = t_E/t_F = \theta rL(N_0\eta H^2)^{-1} = \theta d(L/W)(S\eta^2)^{-1}, \tag{25}$$

where θ is an unknown constant that absorbs the factor of 2 in (24). An appropriate adjust-ment to (21a) is then

$$E_F = \left[(1 - \gamma)e^{-q} + \gamma\right]E_0 \equiv \sigma E_0, \tag{26}$$

with γ given by (22). This form leaves the estimated EKE_M unchanged (relative to $d = 0$) if the dissipation time is long as compared with eddy growth time, and it reverts to (21a) if the dissipation time scale is short as compared with the eddy growth time.

The final proposed scaling (26) is evaluated directly using the 23 paired numerical runs in Table 4 and their twin runs having $d = 0$. The values $\theta = 80$, $c = 2$ and $\mu = 2$ yield a fit with an rms EKE_M error of 0.36×10^{-3} m^2 sec^{-2} and a correlation of 0.94 (Fig. 12). Using the frictionally corrected scaling E_F (26) with all 58 baroclinically unstable model runs yields a fit for EKE_M having correlation of 0.99 and an rms error of 0.60×10^{-3} m^2 sec^{-2}. Thus the revised EKE_M scaling (26) accounts for bottom frictional effects fairly effectively.
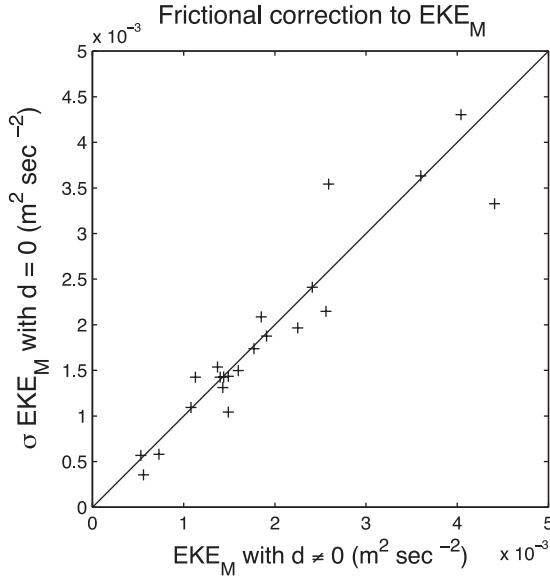
Figure 12. Results of the scaling of maximum eddy kinetic energy to account for bottom frictional effects (26). The horizontal axis displays EKE_M for runs with nonzero bottom stress ($d \neq 0$). The vertical axis shows an approximation to the measured EKE_M estimated using the σ factor times EKE_M from the appropriate matched $d = 0$ run. For example, EKE_M for frictional run 56 is estimated by σ times EKE_M for run 2 (which has $d = 0$). The correlation is 0.94 and the rms error of the comparison is 0.36×10^{-3} m^2 sec^{-2}.

c. Lateral mixing coefficients

Following Brink (2012), the lateral exchange coefficients K are found to scale as a typical eddy speed times a typical length scale (internal Rossby radius). Further, an empirical function of s is included to account for lateral mixing being inhibited by a bottom slope. Specifically, the parameterization K_H for the lateral mixing coefficient is

$$K_H = G E_F^{1/2} \Lambda \eta (1 + C s^2)^{-1}. \tag{27}$$

Note that this s dependence differs slightly from that in Brink (2012): it goes as s^2 rather than $|s|$. Minimizing the squared error in (27) (using all 58 baroclinically unstable runs) leads to the parameters $G = 0.87$ and $C = 30$, a correlation of 0.85 and rms error of 160 m^2 sec^{-1}. The parameterization (27) is certainly not very tight, at least partly because of the 30% noisiness of the model's K estimates (9).

5. Conclusions

The common thread through the new examples here is that the model runs all undergo an initial phase of symmetric instability, either in the interior or in the bottom boundary layer,

or both. Given the nature of this instability (feeding off of shear rather than gravitational potential energy, and only within a confined unstable region), the initial slantwise convection does not significantly affect the available potential energy nor the eventual baroclinic instability. This is demonstrated by the scaling for maximum eddy kinetic energy in the absence of bottom friction (20), which works as well whether or not symmetric instabilities are present. Thus, the more positive results here are not so much about symmetric instabilities *vis-à-vis* baroclinic instability, but rather about eddy evolution in the presence of bottom friction.

Baroclinic instability is never completely halted by frictional effects in any of the cases considered here. However, the inclusion of bottom friction generally weakens baroclinic instability, as measured by either the initial growth rate or by maximum eddy kinetic energy. The consequent finite amplitude eddies show the signature of stratified spindown (e.g., Holton, 1965a) in that the lower part of the interior water column, through a thermal wind balance, has decreased velocities. This vertically sheared structure means that the flow can never become barotropic, so that the inverse scale cascade, which characterizes runs with no bottom friction, cannot go to a large-scale, depth-independent completion when bottom friction is present. Related to this halted cascade is the evolution of mean (associated with alongshore average velocity) kinetic energy. In the absence of bottom friction, mean kinetic energy always increases during the cascade evolution (e.g., Fig. 2), but with bottom friction, the mean kinetic energy decreases relative to initial conditions. This reduction is apparently partly due to direct frictional decay, and partly to the stymied inverse cascade.

Bottom friction causes velocities in the lower part of the water column (and above the bottom boundary layer) to decrease toward zero. This is reflected (e.g., in Fig. 6) in a tendency for currents to be more surface-intensified, even in situations where the flow would otherwise be bottom-intensified. This sort of adjustment, which acts to minimize bottom stresses, is known to occur in linear problems (e.g., Allen, 1984; Power *et al.*, 1989; Brink, 2006) where the stratification or topography allows enough flexibility for the modal structure to adjust. Further, Arbic and Flierl (2004) used a two-layer quasigeostrophic model of an ocean eddy field to show that the same sorts of adjustment can occur in a situation that is fundamentally nonlinear. The present results extend this outcome to a nonlinear case with continuous stratification and where the quasigeostrophic approximation is not valid: there is nothing about (26) that is specific only to eddies originating at a tidal mixing front. Continuous stratification allows a clear separation between boundary layer and interior adjustments, as well as a demonstration of the implications for lateral and vertical scales. Thus, consistent with the results of Arbic and Flierl (2004), it seems likely that bottom frictional effects play an important role in determining the vertical structure of ocean currents throughout the water column, for a wide range of settings extending well beyond the case of an initial tidal mixing front.

Because the frictional energetic adjustment (26) appears to have broader validity, it is worth making at least a qualitative comparison to mid-ocean observations. Specifically, if it were true that bottom friction generally leads to eddy motions that have vanishing velocity

just above the bottom boundary layer, there would be a phase locking between barotropic and baroclinic modes, i.e., the barotropic and baroclinic modes at the bottom would have to sum to zero at all times. This cancelation would occur on time scales on the order of a spindown time, $O(H/r) = O(1$ year or longer) for the deep ocean. The modal coupling would presumably tend to enhance near-surface kinetic energy because of the sign change in the first baroclinic mode.

This is exactly the problem addressed by Wunsch (1997), who systematically used mooring data to study velocity modal structures in the global deep ocean. He showed, using his "ratio" variable (which estimates surface kinetic energy relative to what it would be if the modes were not phase locked), that at most locations there seems to be phase locking but that it acts both constructively and destructively with comparable frequency. One could imagine re-doing these calculations to concentrate only on lower frequencies, and, as Wunsch points out, one can question the statistical certainty of his results at a given location. A reviewer also points out that it is quite possible that Wunsch's results are problematic because modes also couple when the bottom is not flat, which is often the case in the ocean. Thus, Wunsch (1997) does not support the idea that bottom friction causes surface intensification. It appears that really reliable observational results for the present question would entail the use of very long (many years') records only from locations above a flat bottom.

REFERENCES

Allen, J. S. 1984. A simple model for stratified shelf flow fields with bottom friction. J. Phys. Oceanogr., *14*, 1200–1214.

Allen, J. S. and P. Newberger. 1996. Downwelling circulation on the Oregon continental shelf. I. Response to idealized forcing. J. Phys. Oceanogr., *26*, 2011–2035.

Allen, J. S. and P. Newberger. 1998. On symmetric instabilities in oceanic bottom boundary layers. J. Phys. Oceanogr., *28*, 1131–1151.

Arbic, B. K. and G. R. Flierl. 2004. Baroclinically unstable geostrophic turbulence in the limits of strong and weak bottom Ekman friction: Application to midocean eddies. J. Phys. Oceanogr., *34*, 2257–2273.

Badin, G., R. G. Williams, J. T. Holt and L. J. Fernand. 2009. Are mesoscale eddies in shelf seas formed by baroclinic instability of tidal fronts? J. Geophys. Res., *114*, C10021, doi:10.1029/2009JC005340.

Barth, J. A. 1989. Stability of a coastal upwelling front. 2. Model results and comparison with observations. J. Geophys. Res., *94*, 10,857–10,883.

Brink, K. H. 2006. Coastal-trapped waves with finite bottom friction. Dynam. Atmos. Oceans, *41*, 172–190.

Brink, K. H. 2012. Baroclinic instability of an idealized tidal mixing front. J. Marine Res., *70*, 661–688.

Brink, K. H. 2013. Instability of a tidal mixing front in the presence of realistic tides and mixing. J. Marine Res., *71*, 227–251.

Charney, J. G. and M. Stern. 1962. On the stability of internal baroclinic jets in a rotating atmosphere. J. Atmos. Sci., *19*, 159–172.

Haidvogel, D. B., H. G. Arango, K. Hedstrom, A. Beckmann, P. Malanotte-Rizzoli and A. F. Shchepetkin. 2000. Model evaluation experiments in the North Atlantic Basin: Simulations in nonlinear terrain-following coordinates. Dyn. Atmos. Oceans, *32*, 239–281.

Holopainen, E. O. 1961. On the effect of bottom friction in baroclinic waves. Tellus, *13*, 363–367.

Holton, J. R. 1965a. The influence of viscous boundary layers on transient motions in a stratified rotating fluid. I. J. Atmos. Sci., *22*, 402–411.

Holton, J. R. 1965b. The influence of viscous boundary layers on transient motions in a stratified rotating fluid. II. J. Atmos. Sci., *22*, 535–540.

James, I. D. 1989. A three-dimensional model of circulation in a frontal region of the North Sea. Dtsch. Hydrogr. Z., *42*, 231–247.

LaCasce, J. H. and K. H. Brink. 2000. Geostrophic turbulence over a slope. J. Phys. Oceanogr., *30*, 1305–1324.

Larichev, V. D. and J. C. McWilliams. 1991. Weakly decaying turbulence in an equivalent-barotropic fluid. Phys. Fluids A, *3*, 938–950.

Loder, J. W., K. F. Drinkwater, N. S. Oakey and E. P. W. Horne. 1993. Circulation, hydrographic structure and mixing at tidal fronts: The view from Georges Bank. Phil. Trans.: Physical Sciences and Engineering, *343*, 447–460.

Pasquet, A., T. Szekely and Y. Morel. 2012. Production and dispersion of mixed waters in stratified coastal areas. Continental Shelf Research, *39–40*, 49–77.

Pedlosky, J. 1964a. The stability of currents in the atmosphere and oceans. I. J. Atmos. Sci., *27*, 201–219.

Pedlosky, J. 1964b. The stability of currents in the atmosphere and oceans. II. J. Atmos. Sci., *27*, 342–353.

Pedlosky, J. 2014. Symmetric instability of cross-stream varying currents. J. Marine Res., *72*, 31–45.

Power, S. B., J. H. Middleton and R. H. J. Grimshaw. 1989. Frictionally modified continental shelf waves and the subinertial response to wind and deep-sea forcing. J. Phys. Oceanogr. *19*, 1486–1506.

Simpson, J. H. and J. R. Hunter. 1974. Fronts in the Irish Sea. Nature, *250*, 404–406.

Simpson, J. H. and I. D. James. 1986. Coastal and estuarine fronts, *in* Baroclinic Processes on Continental Shelves, C. N. K. Mooers, ed., American Geophysical Union, Washington, DC, 63–94.

St. Maurice, J. P. and G. Veronis. 1975. A multi-scaling analysis of the spin-up problem. J. Fluid Mech., *68*, 417–445.

Stone, P. H. 1966. On non-geostrophic baroclinic instability. J. Atmos. Sci., *23*, 390–400.

Thomas, P. J. and P. F. Linden. 1996. A laboratory model simulation of mixing across tidal fronts. J. Fluid Mech., *309*, 321–344.

Vallis, G. K. and M. E. Maltrud. 1993. Generation of mean flows and jets on a beta-plane and over topography. J. Phys. Oceanogr., *23*, 1346–1362.

van Heijst, G. J. F. 1986. On the dynamics of a tidal mixing front, *in* Marine Interfaces Ecohydrodynamics, J. C. J. Nihoul, ed., Elsevier Oceanography Series, *42*, 165–194.

Wijesekera, H. W., J. S. Allen and P. Newberger. 2003. A modeling study of turbulent mixing over the continental shelf: Comparison of turbulent closure schemes. J. Geophys. Res., *108 (C3)*, 3103, doi:10.1029/2001JC001234.

Wunsch, C. 1997. The vertical partition of oceanic horizontal kinetic energy. J. Phys. Oceanogr., *27*, 1770–1794.